Scanning-tunneling microscopy/spectroscopy and break-junction tunneling spectroscopy of FeSe$_{1-x}$Te$_x$

T. Ekino and A. Sugimoto

Hiroshima University, Graduate School of Integrated Arts and Sciences, Higashi-Hiroshima 739-8521, Japan
E-mail: ekino@hiroshima-u.ac.jp

A.M. Gabovich

Institute of Physics, National Academy of Sciences of Ukraine, 46 Nauka Ave., Kyiv 03028, Ukraine

The iron-chalcogenide superconductor FeSe$_{1-x}$Te$_x$ ($0.5 < x < 1$) was investigated by scanning-tunneling microscopy/spectroscopy (STM/STS) and break-junction techniques. In the STM topography of the samples, randomly distributed Te and Se surface atomic structure patterns correlate well with the bulk composition, demonstrating that nanoscale surface features directly reflect bulk properties. The high-bias STS measurements clarified the gap-like structure at ≈ 100–300 meV, which is consistent with the break-junction data. These high-energy structures were also found in sulfur substituted FeS$_{0.1}$Te$_{0.9}$. Possible origin of such spectral peculiarities is discussed. The superconducting gap $2\Delta \approx 3.4 \pm 0.2$ meV at temperature $T = 4.2$ K was found in the break junction of FeSe$_{1-x}$Te$_x$ with the critical temperature $T_c \approx 10$ K. The corresponding characteristic gap to T_c ratio $2\Delta/k_B T_c \approx 4 \pm 0.2$ indicates moderate superconducting coupling (k_B is the Boltzmann constant).

1. Introduction

The discovery of iron-arsenide superconductor LaFeAsO$_{1-x}$F$_x$ exhibiting $T_c = 26$ K in 2008 [1] stimulated the subsequent synthesis of novel iron-based superconductors, e.g., LiFeAs [2], BaFe$_2$As$_2$ [3], and Fe(Se,Te) [4]. In particular, SmFeAsO$_{1-x}$F$_x$ compound has the highest $T_c \approx 55$ K [5–8], which is a record among non-cuprate superconductors. As for the microscopic Cooper pairing mechanism supporting such high T_c's, several possible candidates were proposed [9,10] and until now it is unclear which of them is a true one.

Among iron-based superconductors there is a PbO type β-FeSe with the simplest crystal structure. Its specific feature, especially beneficial for surface studies, is a good cleavability over the *ab*-plane. The sample surface is believed to be so stable that it is not expected to be reconstructed. The superconductivity of FeSe maintains against substitution of the chalcogenide ions such as Fe(Se,M) (M = Si, Sb, S, Te) [11,12], and Fe(Te,S) [13]. For in-

stance, T_c of Te substituted compound Fe(Se,Te) can be easily manipulated by changing the Se/Te composition ratio. In particular, T_c of FeSe is enhanced up to ~15 K by replacing Se by Te, which has the larger ion radius, while T_c of FeSe is only 8 K. Furthermore, T_c rises up to 37 K under the high pressure of 8.9 GPa [14], which is especially remarkable because such a high critical temperature occurs in a pure binary compound system. Therefore, it seems very important to investigate gradual composition changes and their influence on superconductivity microscopically, e.g., as a function of the Se/Te ratio.

In this paper, single crystals of Fe$_{1.01}$Se$_{1-x}$Te$_x$ ($x = 0.5$–1) were investigated by means of the scanning tunneling microscopy (STM) and spectroscopy (STS), and the results of the nanoscale surface measurements within the large Te range were compared and discussed. The tunneling spectroscopy measurements of the superconducting gapping were also carried out by the break-junction (BJ) method which is extremely sensitive to the electronic spectrum variations in the superconducting state.

2. Experimental

Fe$_{1.01}$Se$_{1-x}$Te$_x$ single crystals were synthesized by a standard process [15]. The mixed powder of Fe, Se, and Te pressed into pellet was double-sealed in an evacuated quartz tube, which was held at 1000 °C for 36 hours to cool down to 400 °C at a rate of –3 °C/h, followed by furnace cooling to room temperature, T. The pristine samples thus obtained were annealed at 400 °C for 100 hours. The electron probe micro analyzer (EPMA) was employed to determine the actual composition of the crystal. The resistivity measurements were done by a standard dc four probe method.

The STM apparatus used in this experiment was an Omicron LT-UHV-STM system, which has been modified to further reduce external disturbance of the sample [16,17]. The sample was cleaved along the layer *in situ* at $T = 77$ K in an ultra-high vacuum (UHV) sample preparation chamber of ~10^{-8} Pa to avoid any contamination or migration of atoms on the crystal surface. The Pt/Ir wire was used as the tunneling tip, which was cleaned by a high-voltage field emission process with Au single crystal target before the scanning operation. The STM measurements were carried out at $T = 4.9$–77 K under the UHV condition of ~ 10^{-8} Pa evacuated by the ion pump. A constant current mode was adopted to obtain the STM images. The BJ tunneling spectra were measured using an ac modulation technique with lock-in amplifier. By this method, fresh and clean superconductor–insulator–superconductor (SIS) junction interface can be obtained along the crack of the thin platelet single crystal at $T = 4.2$ K [18,19].

3. Results and discussion

Prior to the STM/STS measurements, we determined the composition ratio x from EPMA in Fe$_{1.01}$Se$_{1-x}$Te$_x$ with $0.5 < x < 1$ (hereafter, we denote it as FeSe$_{1-x}$Te$_x$). The results showed that the analyzed compositions of Te and Se were in a good agreement with nominal x. The found Te content exceeded x in the range $0.2 < x < 0.5$. The analyzed Fe content 1.02 was slightly larger than the nominal value of 1.01. Single crystals of nominal $x < 0.2$ were not obtained in the present synthesis procedures. From the temperature dependence of resistivity, the maximum T_c was determined: T_c (onset) = 15.9 K, $T_c(0) = 14.5$ K for $x = 0.5$. The critical temperature decreases with either increasing or decreasing x from 0.5. The lowest onset T_c was found as ~ 11 K for $x = 0.9$. In the T-dependence of resistivity for the annealed FeTe sample ($x = 1$), a noticeable drop in the resistivity, which is related to the tetragonal-to-orthorhombic structural phase transition, was observed at around 72 K [20–23]. As the Te content x decreases, the resistivity-drop temperature also goes down accompanying the increase of resistivity. Such a feature was not observed for $x = 0.9$ before the annealing process.

Before the STM measurements, we confirmed the surface electronic cleanliness by measuring the dependence of tunneling current I on the tip-sample distance z, $I(z)$. Figure 1 shows that $I(z)$ curve is exponential. From the perfect linearity of the $\log I$-z dependence, the local work function, $\varphi = 5.2$ eV, is determined. The spatial resolution of the tip was ascertained by monitoring the atomic structures of gold single crystal during the tip preparation process. For the STM measurements, the sample bias voltage $V = \pm 0.01$–0.8 V and the tunneling current $I_t = 0.3$–0.4 nA were adopted as the feedback conditions, but the results did not substantially depend on these parameters. The STM images did not depend on the annealing process. Clear surface spots of atomic arrangements forming the square-lattice structures were always observed. The period of lattice spot structures is ~ 0.37–0.38 nm for all compositions x, thus no distinguishable differences were found among them within the resolution.

The STM images for FeSe$_{1-x}$Te$_x$ with various x measured at 4.9 K are shown in Fig. 2. Since the crystal structure consists of the stacking of edge-sharing FeSe$_4$ tetrahedral layers, the cleaved surface is always the same. This is very advantageous for the investigation of the *ab*-plane properties in this compound. They exhibit the coexistence of the bright and dark spots for all the topographies. In Fig. 2(a), bright and dark spots are shown to be randomly distributed over the wide area of the atomic image. Such coexistence is realized only for the limited range of compositions x, where bright and dark spots correspond to Te and Se atoms, respectively, as was discussed earlier [15]. Similar STM images were also reported in Refs. 24–27.
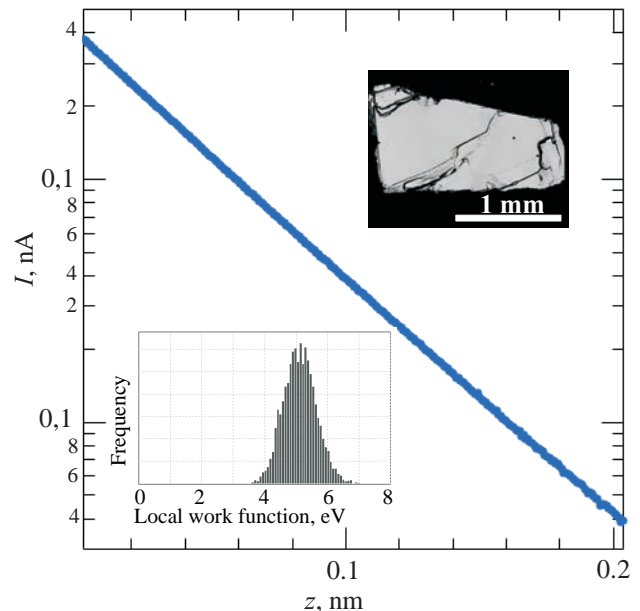

Fig. 1. Dependence of the tunneling current I on the tip-sample distance z between PtIr tip and FeSe$_{1-x}$Te$_x$ single crystal. The upper-right inset shows the optical micrograph of the single crystal, while the lower left inset displays a histogram of the local work function (the barrier height).
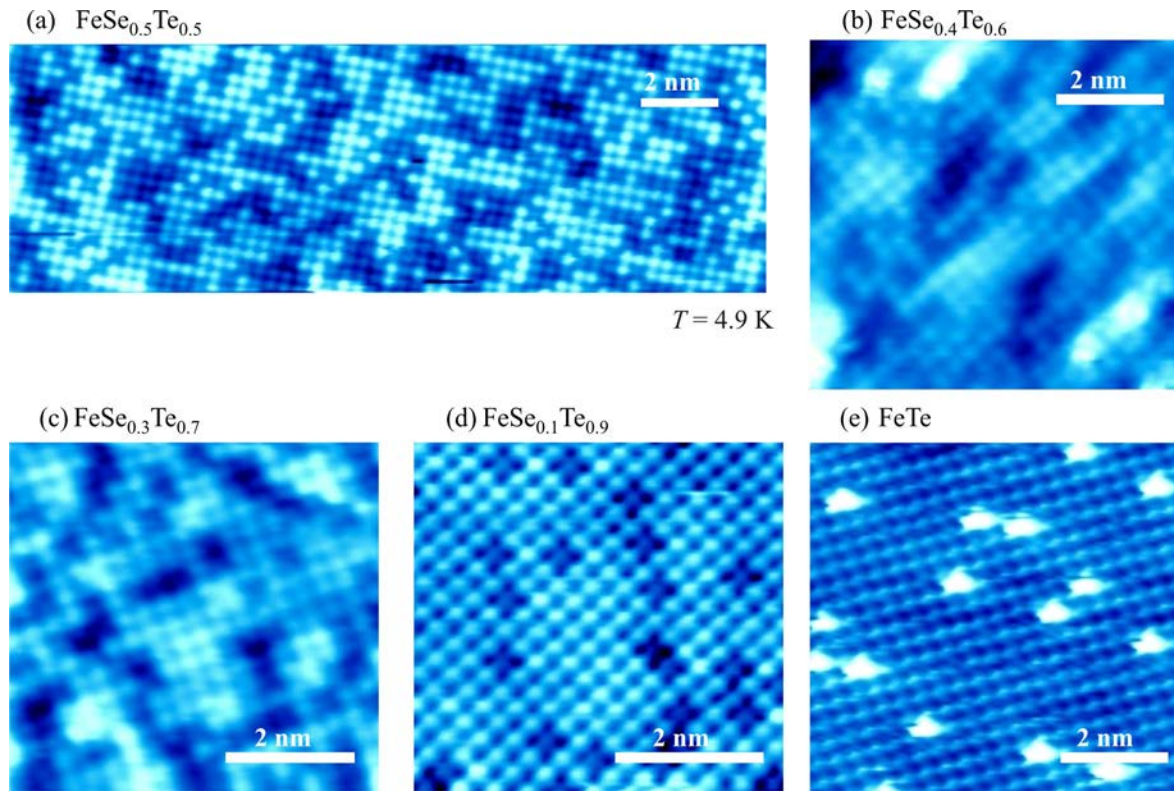
Fig. 2. STM topography of $FeSe_{1-x}Te_x$ for $0.5 < x < 1$. $T = 4.9$ K, $I = 0.3$ nA, $V = -0.4$ V.

The dynamic range of the topographic contrast slightly depends on the frames. The bright spots are located just on the atomic grid points of the square lattice structure for $x = 0.5$–0.9 (Figs. 2(a)–(d)), while the bright shining spots shown for $x = 1$, Fig. 2(e), seem to be slightly away from the formal atomic positions and extend to a few atoms. Therefore, the origin of these spots in Fig. 2(e) is probably different from that of the bright spots in Figs. 2(a)–(d). By assuming these spots in Fig. 2(e) as excess Fe atoms, the clusters are counted in the larger area of topography, and the ratio of ~ 0.05 was obtained. This is consistent with the data from EPMA. The atomic spots in Fig. 2(e) except the discussed Fe spots are homogeneous, which are naturally attributed to Te atoms. Interestingly, Te atoms as the brighter spots in Figs. 2(a)–(d) turn into the darker spots in Fig. 2(e), but it is understood if we consider the difference in the atomic sizes (Te atom having larger size than Se one) for Figs. 2(a)–(d) or the height of the excess Fe atoms on the surface for Fig. 2(e), respectively, which results in relative change in the contrast.

A direct evidence of distinguishing atoms in line with the discussion is given in Fig. 3, where the STM topography and its cross section along the indicated line is presented for $x = 0.7$ and $x = 0.9$. The ripple patterns reflecting the sample-tip distance being kept constant are readily seen in the cross sectional profiles. The positions of spiky dips among the regular shallow ripples in the height profiles in Figs. 3(a) and (b) correspond to the darker spots in

the topography. The depth of the spikes is ~ 0.02–0.03 nm for both profiles. Since the ionic radii of Te and Se are 0.221 and 0.198 nm, respectively, the difference in the height z reflects just the difference of ionic radii ≈ 0.023 nm between Te and Se. Therefore, the difference in ion sizes between them is now visualized. Figure 3(c) shows the dark-spot ratio in the STM images *versus* the Se content $(1-x)$ determined from EPMA. The dark-spot ratio was defined by counting the numbers of dark n_d and bright n_b spots within the area of typically 30×30 nm and then normalized as $n_d/(n_b + n_d)$. The bright shinning spots discussed above were sometimes observed in the whole x ranges, but they were omitted from the counting. Almost perfect linear relationship was obtained between the dark-spot ratio on the STM image and the Se content taken from EPMA. From these results, we identify the origin of the bright and dark spots in the whole investigated range of $0.5 < x < 0.9$. The results testify that the bulk characteristics directly correlate with the nanoscale local features of the freshly cleaved crystal surface. These convincing topographic studies with atomic resolution are ensured by the high quality of the local tunnel barriers manifested by the constancy of the measured work function.

In spite of such clear observations of the surface atomic arrangements of $FeSe_{1-x}Te_x$ with precise identification of Te and Se atoms on the crystal surface, we observed by STS no clear local superconducting gaps. The electronic surface inhomogeneity might be a possible primary origin
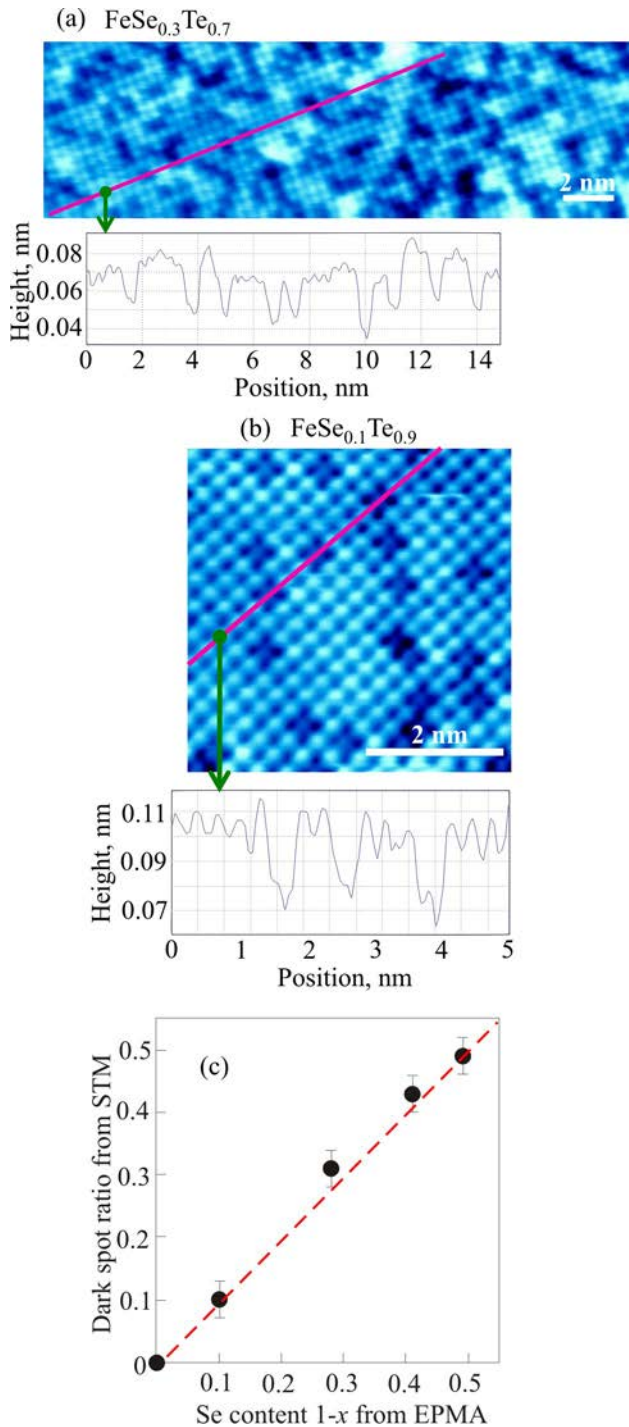
(a) FeSe$_{0.3}$Te$_{0.7}$

(b) FeSe$_{0.1}$Te$_{0.9}$

Fig. 3. Line profiles of the STM topography for FeSe$_{0.3}$Te$_{0.7}$ (a) and FeSe$_{0.1}$Te$_{0.9}$ (b). Dark spot ratio from STM *versus* Se content (1–*x*) from the electron-probe micro analyzer (EPMA) (c).

of the obscure superconducting gap structures. To confirm such a nanoscale electronic irregularity we built STS conductance mappings.

Figure 4 demonstrates the STM topography and the mapping of the differential conductance *dI/dV* at zero bias and *V* = 30 mV for FeSe$_{0.3}$Te$_{0.7}$ in the superconducting state at 4.9 K. The patch-like patterns in the conductance map of 5×5 nm roughly resemble those of STM topogra-

phy in the same region, which is due to Te/Se distributions as indicated in Fig. 2. However, a closer look indicates slight discrepancies between the contrast patterns of the topography and conductance mapping. This can be explained by the manifestation of the local density of states integrated over the energy revealed in the topography while density of states itself determines the conductance mapping. To clarify this point further, the line profiles of the conductance are shown for the line cuts from three different locations. The conductance magnitude becomes remarkably inhomogeneous when the bias voltage exceeds +20–30 mV while it is fairly homogeneous for the negative bias. This indicates the existence of impurity states in the empty band. Since the energy scale of the inhomogeneity starting at 20–30 meV is much higher than $T_c \sim 10$ K (~ 0.9 meV) of FeSe$_{0.3}$Te$_{0.7}$, it does not seem to be directly related to the superconducting properties. The Bardeen-Cooper-Schrieffer (BCS) pairing energy is about ≈ 2 meV, but no trace of a superconducting gap is seen in any of local conductance profiles in the low bias regions below 10 mV.

It stems from the figure that there are no serious local nanoscale inhomogeneities at zero bias which would be able to smear superconducting-like spectra with their small energy gaps. (This is in contrast to the pattern at $V > 20$–30 meV where the substantial irregularity does exist.) The gap-related features might have been washed out by surface variations of the electronic properties emerging despite low-*T* and UHV cleaving conditions. Nevertheless, it is impossible now to indicate any sound reason of such variations. One might also consider the absence of gapping being due to bad resolution of the STS chamber. However, measurements with the same STM/STS apparatus demonstrated conspicuous atomic arrangements and the superconducting gap features in the other layered superconductor β-ZrNCl having a similar $T_c = 13$–15 K [28].

The existence of the superconducting gap could be found by examination of the zero-bias conductance in the superconducting state. Corresponding attempts were made and the results obtained are shown in Fig. 4, in which the dark-contrast region near zero-bias corresponding to the depression of the electronic density of states might be due to the manifestation of the superconductivity gap, because such deep dark contrast becomes generally weak upon warming. Anyway, there are no traces of the apparent gap structure in the observed line profiles.

Hence, another effective method of BJ tunneling spectroscopy (BJTS) [18] was applied to reveal superconducting gaps in the materials concerned. In this technique, the symmetric geometry of electrodes is realized so that the overwhelming majority of junctions are of the SIS nature. Since the crack section is perpendicular to the plate the tunneling current passes mainly through the *ab* crystal plane.

Quite a number of iron-based superconductors are believed to manifest multiple or anisotropic gaps [29] as a consequence of the multiple electronic band structure [10].
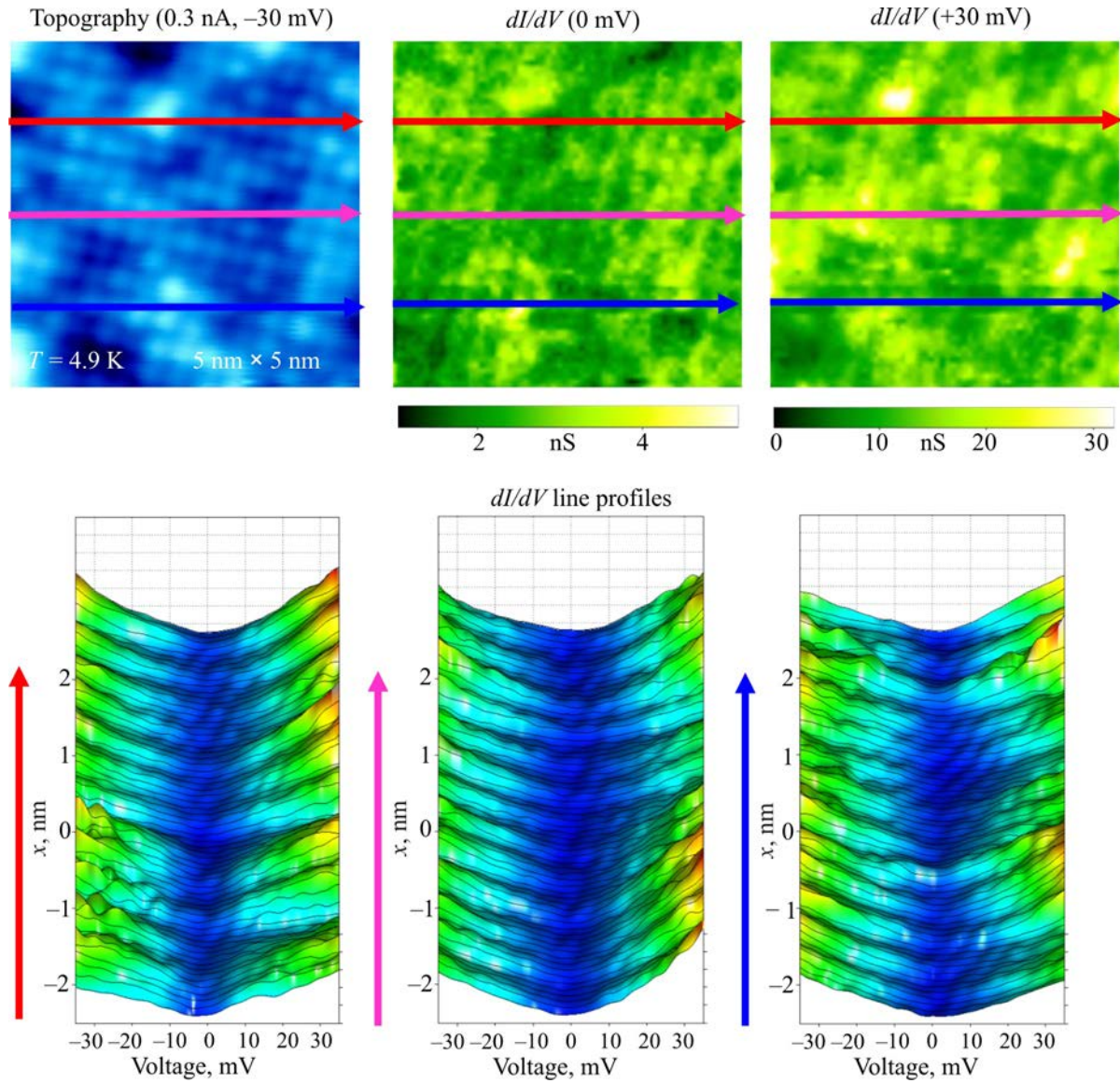
Fig. 4. The STM topography, the *dI/dV* mapping, and the *dI/dV* line profiles for FeSe$_{0.3}$Te$_{0.7}$ at 4.9 K.

In particular, two-gap behavior was demonstrated in FeSe$_{1-x}$ [30]. We sought for this phenomenon in our samples of FeSe$_{1-x}$Te$_x$ but succeeded in the observation of the maximum-gap features only. This major gap, which is of the order of T_c if the gaps are relatively weakly coupled, is a parameter that at least approximately reflects the strength of the pairing interaction [31].

Figure 5(a) shows three representative BJ tunneling conductances measured at $T = 4.2$ K for FeSe$_{0.5}$Te$_{0.5}$, which possesses the highest bulk $T_c = 15$ K among the series FeSe$_{1-x}$Te$_x$. The top curve shows a conspicuous depletion of the electron density of states as well as inexpressive conductance peaks. The pattern can be associated with the presence of the superconducting gap. The gap smearing correlates with a large observed zero-bias leakage conductance as compared to the standard BCS density of states.

At the same time, the middle and bottom curves in Fig. 5(a) reveal more subtle gap-like features demonstrating hints of multigapness. The inner coherent peaks of the double-gap structure in the middle curve correspond to the gap peaks of the top curve positioned at ± 2–3 mV, while the outer ones correlate with the rather strong peaks of the bottom curve positioned at ± 5–6 mV. Since the latter bias voltages are twice as much as the former ones, a plausible conclusion may be made that the outer and inner peaks are generated by tunneling through SIS (the bottom curve) and SIN (the top curve, *N* stands for a normal metal) junctions, respectively rather than by random scatter of multiple gap values due to the sample inhomogeneity. Indeed, SIN junctions are often formed instead of SIS counterparts even in symmetric break junctions. This can be understood as the consequence of the crack occurrence at a crystal defect or grain boundary [32].
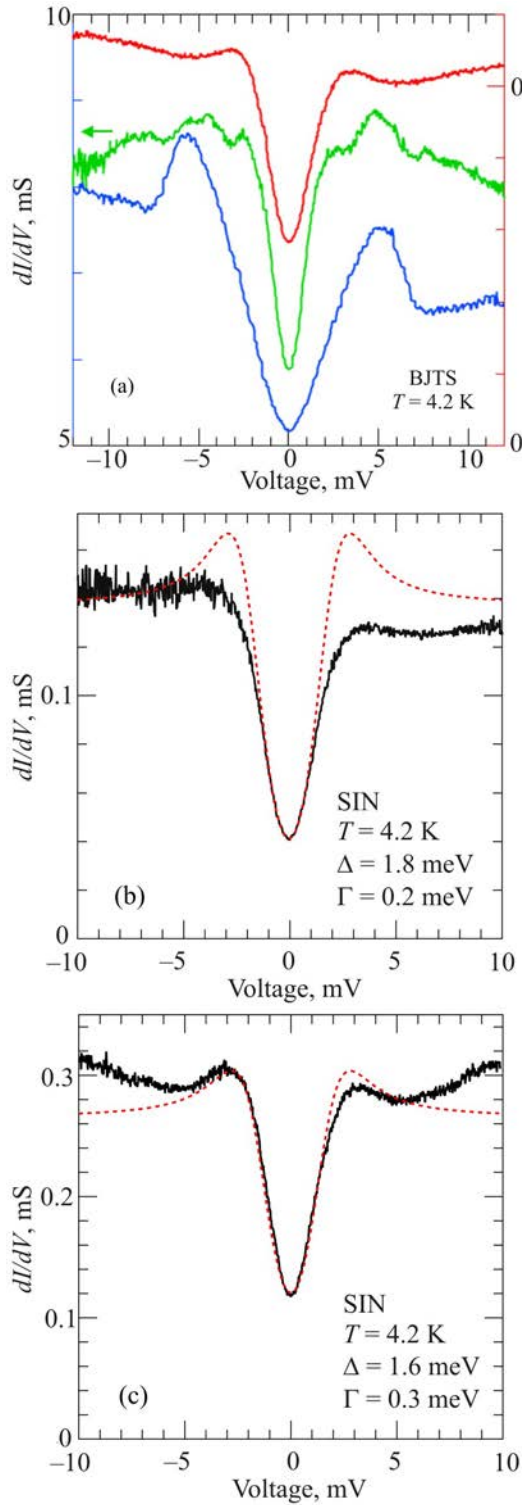
Fig. 5. The *dI/dV* curves of FeSe$_{0.5}$Te$_{0.5}$ (a) at 4.2 K from break-junction tunneling spectroscopy (BJTS). The *dI/dV* fittings using the broadened BCS density of states (dotted curves) (b) and (c).

The above arguments were checked by the conductance fitting using the broadened BCS density of states with the account of thermal broadening. In the fitting, the well-known approximation for the density of states, $N(E, \Gamma) = |\text{Re}\{(E - i\Gamma)/[(E - i\Gamma)^2 - \Delta^2]^{1/2}\}|$, was used, where Γ and Δ are the phenomenological broadening and gap parame-

ters, respectively [33]. The fitted results are depicted as dashed lines in Figs. 5(b) and (c). The overall features including the broadened gap peaks and especially the substantial leakage conductance at zero bias are fairly well reproduced. On the other hand, the calculated conductance peaks are much shaper than the experimental data. The best fitting parameters at $T = 4.2$ K are $\Delta = 1.6$–1.8 meV and $\Gamma = 0.2$–0.3 meV, respectively. As for the microscopic origin of Γ, there exist several possible factors such as gap anisotropy, inhomogeneity, etc., although there are no quantitative estimations. On the other hand, relatively large but rather common value obtained here implies the extrinsic interface influence. Such a large Γ value probably reflects the depression of the superconducting gap features in STS. From the fitting results in Figs. 5(b) and (c), in which the correspondence between experimental data and calculated curves is rather good in the zero bias region, the feature of sub-gap conductance seems to have nothing in common with any non-conventional anisotropic pairing.

Figure 6 shows the *T*-dependence of the conductance in the gap region corresponding to Fig. 5(b). The gap structure already broadened at 4.2 K is further broadened upon warming and smeared out at a local $T_c = 10$ K in the junction. This is much lower than the bulk $T_c = 15$ K from the resistivity measurements. The figure also indicates the SIN junction formation in BJ as is indicated in Fig. 5(b), where the gap structure is gradually smeared out but the gap-edge peaks do not shift to zero at $T \to T_c$, which is in contrast to the behavior of SIS junctions [32]. The low-*T* gap value $2\Delta = 3.2$–3.6 meV and the junction local $T_c = 10$ K give the characteristic gap to T_c ratio $2\Delta/k_B T_c = 3.7$–4.2. This is slightly larger than the BCS value ≈ 3.5, indicating a moderate or strong-coupling. Similar gap values were reported in the earlier STS studies [24,25,27].
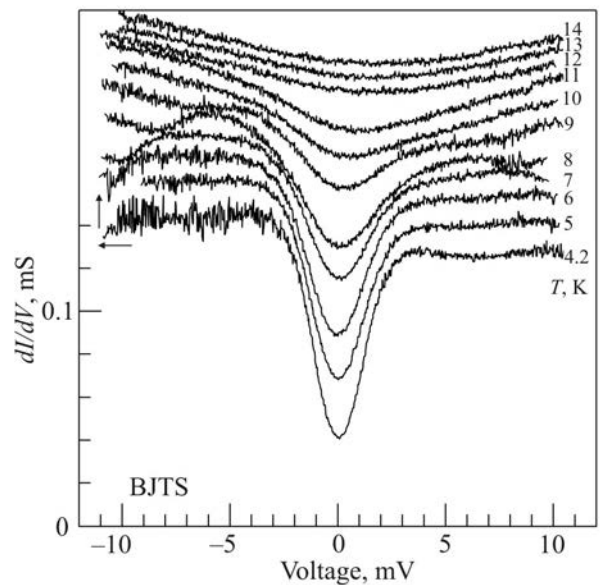

Fig. 6. Temperature evolution of *dI/dV* for FeSe$_{0.5}$Te$_{0.5}$. The conductance is shifted up for the clarity.

In the BJ measurements, substantial variation of both gaps was found. Most probably, it is because BJTS is sensitive to local changes in stoichiometry as described in our previous measurements [34]. These BJ studies reveal an upper limit of the superconducting gap value. The solid curve in Fig. 7(a) shows the maximum gap size observed in this series of measurements, where the peak-to-peak separation of $V_{p-p} \approx 13$–14 mV was obtained in the gap structure with moderately pronounced peaks. This gap may be attributed to the maximum $T_c = 15$ K in this compound series. The representative outer gap structure in Fig. 5(a) is also shown for the comparison. We can recognize that the larger gap size possesses the larger conductance leakage (probably reflecting the low superconducting volume fraction). This is consistent with the fact that we often obtained immature gap size and T_c, as shown in Figs. 5 and 6. This set of thermodynamic parameters correlates well with $V_{p-p} \approx 40$ mV and $T_c \approx 48$ K of the superconducting NdFeAsO$_{0.9}$F$_{0.1}$ found in our BJTS measurements [35], thereby supporting the idea of a common mechanism of superconductivity among the iron-based compounds [10,36].

In fact, one-unit-cell film of FeSe fabricated by molecular beam epitaxy was found to exhibit superconductivity above 50 K and reveals the gap values of ≈ 20 mV and ≈ 40 mV in STS investigations [37,38]. Notwithstanding the difference in T_c, the coherent peak positions in Ref. 37 correlate with our results of $V_{p-p} \approx 40$ mV for the symmetric BJ junction. In Fig. 7(b), superconducting zero-T gap *versus* T_c plots for several iron-based superconductors are shown together with those of some copper oxides as well as of previously investigated by us layered nitrochloride superconductors [28,39]. All the measurements were done by the fixed design of BJTS. The plots demonstrate a remarkable difference in the slope reflecting the difference in the coupling strength and, possibly, in the underlying mechanism of Cooper pairing. Namely, the slope is about the s-wave BCS weak-coupling value in iron-based superconductors, while it is more than twice that in the copper-oxide and nitrochloride superconductors. Therefore, it is clear that cuprates and nitrochlorides possess unusually large energy scale of the pairing interaction, the origin of which remains to be clarified [39,40]. As for cuprates, it might be a consequence of the charge-density-wave (CDW) influence on superconductivity [41].

We have extended the bias voltage range to investigate the background normal-state electronic states. Figure 8(a) shows representative tunneling conductances obtained in both STS (*A* and *B*) and BJTS (*C* and *D*) measurements. The STS conductance is obtained by averaging 4096 spectra in a 10×10 nm region, while the BJTS conductance is a single trace from a junction. The revealed broadened gap-like structure in STS spectra appears to be asymmetric with respect to zero bias, but the bias polarity of the enhanced peak in the asymmetric conductance depends on the mea-
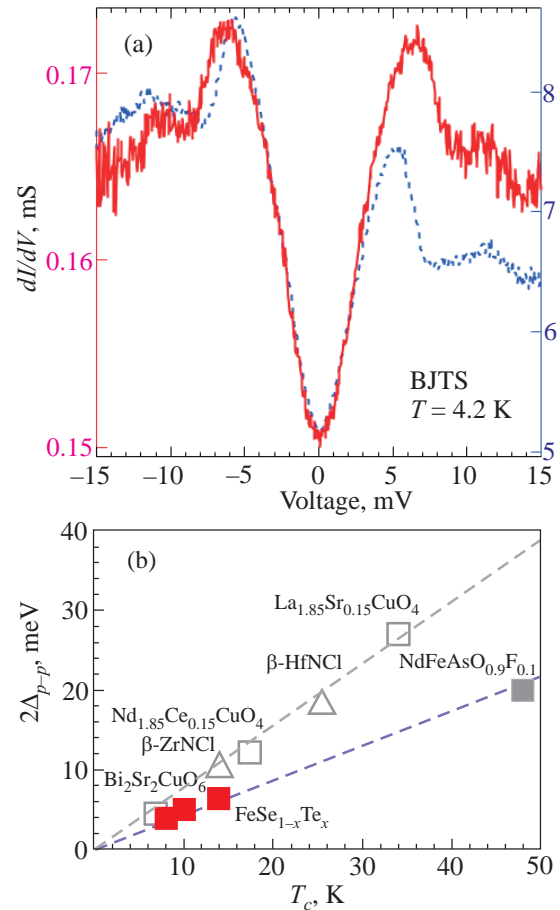

Fig. 7. The maximum gap structure observed in the measurements of FeSe$_{1-x}$Te$_x$ (a). Peak-to-peak value of the superconducting gap $2\Delta_{p-p}$ *versus* T_c(K) for several superconductors [35,38,39] (b).

surement run as shown in two characteristic curves of Fig. 8(a). The asymmetric gap structure of curve *A* possesses a moderately enhanced peak appearing at the negative bias of ~ –300 mV, while a subtle peak at the positive bias ≈ 100 mV becomes distinct only after normalizing by the background value. Note that the bias polarity is defined with respect to the sample. The high-energy gap structures found in STS persist even at 77 K, showing the peaks at –300 mV and +100mV, as displayed in Fig. 8(b).

The sub-gap conductance depends linearly on the bias showing a very weak bend at –100–150 mV, which becomes visible after the normalization. This bias is symmetric with respect to the smaller peak occurring at +100 mV in the normalized conductance, which is distinctly manifested in the raw conductance data of *B* only in the positive bias.

Curves *C* and *D* in Fig. 8(a) describe the high-energy structure of the BJTS conductance similar to that observed by STS. The conductance is reasonably symmetric in accordance with the SIS nature of the junction. The well-distinguished gap-edge structures are seen at $\approx \pm 300$ mV for *C* with small bends at ±100mV, accompanying an in-
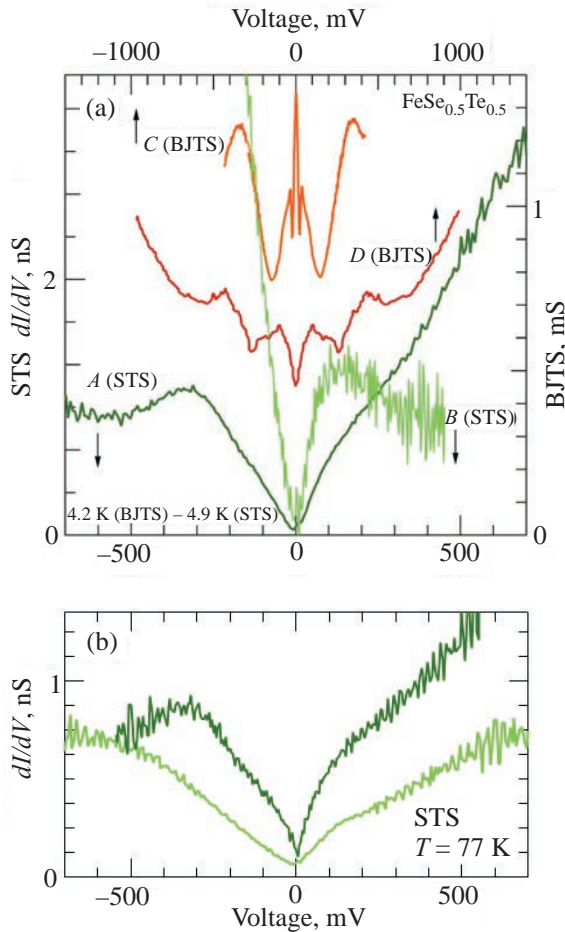
Fig. 8. The *dI/dV* curves for FeSe$_{0.5}$Te$_{0.5}$ obtained from STS (*A*, *B*) and BJTS (*C*, *D*) at *T* = 4–5 K (a), and STS at 77 K (b).

tensive broad zero-bias peak due to a superconducting weak-link behavior of the junction. The broadened double-peak structure is seen in *D* at ±400 mV and ±150 mV, possessing the slightly larger energy than in *C*. These gap features are in agreement with the STS spectra.

The lack of superconductivity manifestations in spectrum *D* is probably due to break of the sample in the non-superconducting region or the gap averaging out by inhomogeneity. This explanation correlates with relatively large conductance leakage. It might also happen that the absence of superconductivity is due to the insufficient resolution of the ac modulation voltage (> 1 mV) in this case.

The line profiles of the conductance mapping are shown in Figs. 9(a) and (b) from the STS measurements at 4.9 K within the length scale of ≈ 10 nm. The broadened peaks at ≈ – 300 mV (Fig. 9(a)) and +100 mV (Fig. 9(b)) are evident anywhere in the spatial region, which demonstrate that the conductance below |*V*| = 400 mV is fairly homogeneous at least in this range with small accidental variations.

The broad peak structure at –300 mV is consistent with the binding energy of 300 meV in the density of states originating from iron *d*-state as observed in the valence-band photoemission spectroscopy [42]. On the other hand, the

conductance peak positions which change with the bias polarity (–300 mV and +100 mV) could be due to the tunneling from different sections of the Fermi surface. In fact, the angle-resolved photoemission spectroscopy along the high-symmetry line of the Brillouin zone showed a broad peak feature at ≈ 300 meV around the Γ point and a nondispersive band at ≈ 100 meV around the *M* point, respectivey [43]. The energies of asymmetric peaks with strongly asymmetric conductance background observed in STS could be explained by the difference in the tunneling probability along the different directions in the Brillouin zone. Since the negative bias corresponds to the electron tunneling from the sample into the tip, the observed peak at –300 mV might reflect the bottom of the electron band, while the +100 mV peak reflects the empty states of the top of the hole like band, both of which are located at the Γ point. The conductance features like this exist in the broad composition range, showing similar nanoscale homogeneity.

The remarkable segmental dependence of the conductance background occurring intensively in the particular surface regions, that is, stronger positive or negative bias dependences in Figs.9(a) or (b), respectively, could hide the peak in the opposite bias. Such features could happen when the shape of the potential barrier plays an important role. In the vacuum tunneling using an STM tip, local enhancement of the electric field modifying the barrier yields a strong bias dependence.

The density-wave formation in the layered compound may be another plausible driving force of the conductance asymmetry as predicted by the theory [44]. As for the gap size observed here, it is typical to those of the charge density wave compounds [45,46]. Specifically, the asymmetry in the gap structure could be a manifestation of the influence of the CDW order parameter phase. This is a possible reason of the pseudogap (dip-hump) peak existence on one bias polarity branch only [47]. The existence of the asymmetric gap feature in the STS conductance could be a smoking gun of the CDW appearance in FeSe$_{1-x}$Te$_x$, which might exist in iron-based compounds along with spin density waves (SDWs) [36]. At the same time, SDW can also promote asymmetry of the tunneling conductance [44].

Assuming the energy scale of the conventional CDW compounds, the present gap might disappear at ≈ 100–250 K. This is in accordance with Fig. 8(b), where the gap-like structures are observed even at 77 K. In fact, the structural phase transition near 90 K has been reported in FeSe [48], and confirmed in our own resistivity measurements [49]. These characteristic features can be associated with high bias gap-like structures observed here.

The high-energy gap like structure is reproduced in the sulfur-substituted compound. Figure 10 shows the STS conductance profile for Fe$_{1.02}$S$_{0.1}$Te$_{0.9}$ where compositions were determined by EPMA. Rather homogeneous line profile in the spatial range of 10 nm is similar to that in the Se-substituted compound. The pronounced peak at
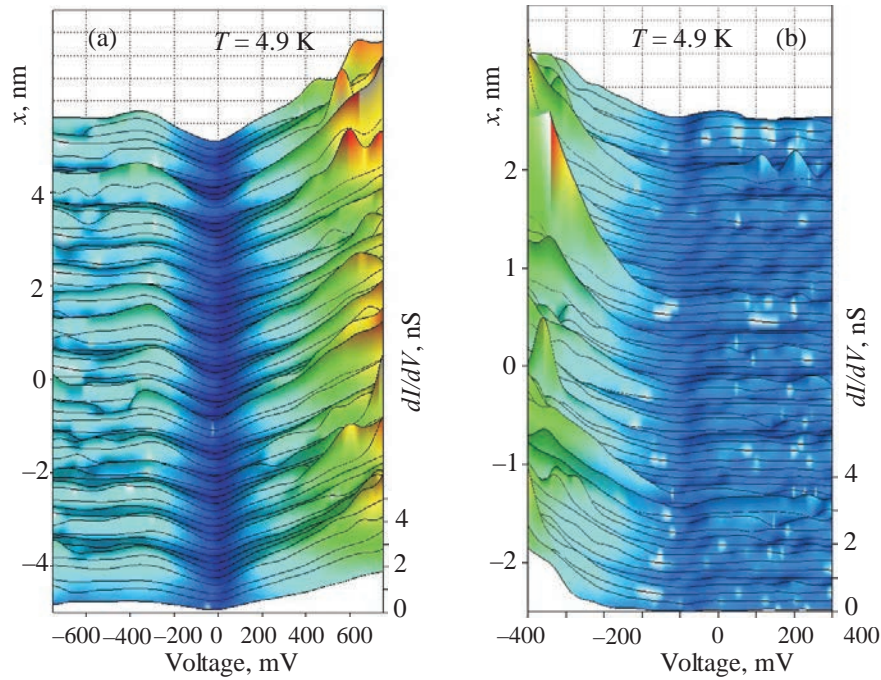
Fig. 9. Line profiles of *dI/dV* for FeSe$_{0.5}$Te$_{0.5}$ measured by STS at 4.9 K, showing the peak at –300 mV (a) and +100 mV (b). The profiles of (a) and (b) were taken from different samples.

≈ –400 mV and a weak structure at +100–200 mV are slightly larger than in the Se compound, but essentially in the same energy range. The difference is probably due to modifications of electronic states upon the change of the ion sizes, since the S ion is 7–9% smaller than the Se one.

In order to study the high-energy feature in connection with the magnetic phase transition at 72 K [20–23], the STS measurements have been carried out for the non-superconducting Fe$_{1.01}$Te. The results showing the shallow
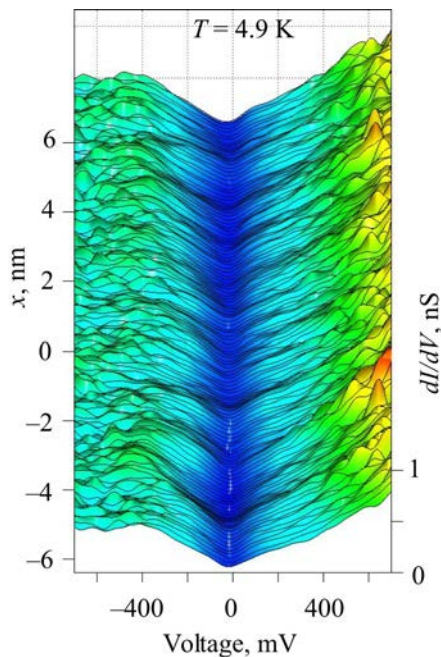
zero-bias depression of conductance and no apparent high-energy gap structure are in contrast to Fig. 8, although both conductance spectra display noticeable asymmetry with respect to the bias voltage. This difference of the observed electronic structures in a normal metal FeTe and a superconductor FeSe$_{1-x}$Te$_x$ is consistent with calculations [50].

4. Summary

We have synthesized and measured the surface and electronic properties of Fe$_{1.01}$Se$_{1-x}$Te$_x$ ($0.5 < x < 1$) single crystals by means of STM/STS and BJ tunneling spectroscopy. The STM topographies distinguish Se and Te atoms in the whole x range, indicating that surface local events directly reflect the bulk properties. The STS and break junction measurements clarified the asymmetric gap-like structure at ≈ ±100 mV and –300 mV. These features seem to be consistent with the photoemission spectra, while the distinct asymmetric gap-like feature can be explained by a possible CDW formation. Such structures are also observed in sulfur substituted Fe$_{1.02}$S$_{0.1}$Te$_{0.9}$, but not in Fe$_{1.01}$Te. The superconducting gap structure is probed by BJ tunneling. A smeared BCS density of states with 2Δ (4 K) ≈ 3.4 ± 0.2 meV for T_c ~ 10 K was observed. The characteristic gap ratio $2\Delta(0)/k_B T_c = 3.7$–4.2 indicates an intermediate superconducting coupling strength.

Acknowledgements

Fig. 10. Line profile of *dI/dV* from STS for FeS$_{0.1}$Te$_{0.9}$ at 4.9 K.

1. Y. Kamihara, T. Watanabe, M. Hirono, and H. Hosono, *J. Am. Chem. Soc.* **130**, 3296 (2008).

2. X.C. Wang, Q.Q. Liu, Y.X. Lv, W.B. Gao, L.X. Yang, R.C. Yu, F.Y. Li, and C.Q. Jin, *Solid State Commun.* **148**, 538 (2008).

3. M. Rotter, M. Tegel, and D. Johrendt, *Phys. Rev. Lett.* **101**, 107006 (2008).

4. F.C. Hsu, J.Y. Luo, K.W. The, T.K. Chen, T.W. Huang, P.M. Wu, Y.C. Lee, Y.L. Huang, Y.Y. Chu, D.C. Yan, and M.K. Wu, *Proc. Natl. Acad. Sci.* **105**, 14262 (2008).

5. X.H. Chen, T. Wu, G. Wu, R.H. Liu, H. Chen, and D.F. Fang, *Nature* **453**, 761 (2008).

6. G.F. Chen, Z. Li, D. Wu, G. Li, W.Z. Hu, J. Dong, P. Zheng, J.L. Luo, and N.L. Wang, *Phys. Rev. Lett.* **100**, 247002 (2008).

7. H.H. Wen, G. Mu, L. Fang, H. Yang, and X. Zhu, *Europhys. Lett.* **82**, 17009 (2008).

8. Z.-A. Ren, J. Yang, W. Lu, X.-L. Shen, Z. Cai Li, G.-C. Che, X.-L. Dong, L.-L. Sun, F. Zhou, and Z.-X. Zhao, *Europhys. Lett.* **82**, 57002 (2008).

9. K. Kuroki, R. Arita, and H. Aoki, *Butsuri* **64**, 627 (2009) (*in Japanese*).

10. A.A. Kordyuk, *Fiz. Nizk. Temp.* **38**, 1119 (2012) [*Low Temp. Phys.* **38**, 888 (2012)].

11. S. Pandya, S. Sherif, L.S.S. Chandra, and V. Ganesan, *Supercond. Sci. Tech.* **24**, 045011 (2011).

12. Y. Mizuguchi, F. Tomioka, S. Tsuda, T. Yamaguchi, and Y. Takano, *J. Phys. Soc. Jpn.* **78**, 074712 (2009).

13. K. Deguchi, Y. Mizuguchi, Y. Kawasaki, T. Ozaki, S. Tsuda, T. Yamaguchi, and Y. Takano, *Supercond. Sci. Tech.* **24**, 055008 (2011).

14. S. Medvedev, T.M. McQueen, I.A. Troyan, T. Palasyuk, M.I. Eremets, R.J. Cava, S. Naghavi, F. Casper, V. Ksenofontov, G. Wortmann, and C. Felser, *Nature Mater.* **8**, 630 (2009).

15. R. Ukita, A. Sugimoto, and T. Ekino, *Physica C* **471**, S622 (2011).

16. A. Sugimoto, T. Ekino, and H. Eisaki, *J. Phys. Soc. Jpn.* **77**, 043705 (2008).

17. A. Sugimoto, K. Shohara, T. Ekino, Y. Watanabe, Y. Harada, S. Mikusu, K. Tokiwa, and T. Watanabe, *Physica C* **469**, 1020 (2009).

18. T. Ekino, T. Takabatake, H. Tanaka, and H. Fujii, *Phys. Rev. Lett.* **75**, 4262 (1995).

19. T. Ekino, A. Sugimoto, H. Okabe, K. Shohara, R. Ukita, J. Akimitsu, and A.M. Gabovich, *Physica C* **470**, 358 (2010).

20. B.C. Sales, A.S. Sefat, M.A. McGuire, R.Y. Jin, and D. Mandrus, *Phys. Rev. B* **79**, 094521 (2009).

21. Y. Mizuguchi, F. Tomioka, S. Tsuda, T. Yamaguchi, and Y. Takano. *Appl. Phys. Lett.* **94**, 012503 (2009).

22. K.W. Yeh, T.W. Huang, Y.L. Huang, T.K. Chen, F.C. Hsu, P.M. Wu, Y.C. Lee, Y.Y. Chu, C.L. Chen, J.Y. Luo, D.C. Yan, and M.K. Wu, *Europhys. Lett.* **84**, 37002 (2008).

23. W. Bao, Y. Qiu, Q. Huang, M.A. Green, P. Zajdel, M.R. Fitzsimmons, M. Zhernenkov, S. Chang, M. Fang, B. Qian, E.K. Vehstedt, J. Yang, H.M. Pham, L. Spinu, and Z.Q. Mao, *Phys. Rev. Lett.* **102**, 247001 (2009).

24. T. Kato, Y. Mizuguchi, H. Nakamura, T. Machida, H. Sakata, and Y. Takano, *Phys. Rev. B* **80**, 180507 (2009).

25. T. Hanaguri, S. Niitaka, K. Kuroki, and H. Takagi, *Science* **328**, 5977 (2010).

26. F. Massee, S. de Jong, Y. Huang, J. Kaas, E. van Heumen, J.B. Goedkoop, and M.S. Golden, *Phys. Rev. B* **80**, 140507 (2009).

27. C-L. Song, Y-L. Wang, P. Cheng, Y-P. Jiang, W. Li, T. Zhang, Z. Li, K. He, L. Wang, J-F. Jia, H-H. Hung, C. Wu, X. Ma, X. Chen, and Q-K. Xue, *Science* **332**, 1410 (2011).

28. A. Sugimoto, K. Shohara, T. Ekino, Z. Zheng, and S. Yamanaka, *Phys. Rev. B* **85**, 144517 (2012).

29. G. R. Stewart, *Rev. Mod. Phys.* **83**, 1589 (2011).

30. R. Khasanov, M. Bendele, A. Amato, K. Coder, H. Keller, H.-H. Klaus, H. Luetkens, and E. Pomjakushima, *Phys. Rev. Lett.* **104**, 087004 (2010).

31. V.Z. Kresin and S.A. Wolf, *Physica C* **169**, 476 (1990).

32. T. Ekino, H. Fuji, T. Nakama, and R. Yagasaki, *Phys. Rev. B* **56**, 7851 (1997).

33. R.C. Dynes, V. Narayanamurti, and J.P. Garno, *Phys. Rev. Lett.* **41**, 1509 (1978).

34. T. Ekino, H. Fujii, M. Kosugi, Y. Zenitani, and J. Akimitsu, *Phys. Rev. B* **53**, 5640 (1996).

35. T. Ekino, A. Sugimoto, H. Okabe, K. Shohara, R. Ukita, J. Akimitsu, and A.M. Gabovich, *Physica C* **470**, S358 (2010).

36. A. Chubukov, *Annu. Rev. Condens. Matter Phys.* **3**, 57 (2012).

37. Q.-Y. Wang, Z. Li, W.-H. Zhang, Z.-C. Zhang, J.-S. Zhang, W. Li, H. Ding, Y.-B. Ou, P. Deng, K. Chang, J. Wen, C.-L. Song, K. He Ke, J.-F. Jia, S.-H. Ji, Y.-Y. Wang, L.-L. Wang, X. Chen, X.-C. Ma, and Q.-K. Xue, *Chin. Phys. Lett.* **29**, 037402 (2012).

38. S. He, J. He, W. Zhang, L. Zhao, D. Liu, X. Liu, D. Mou, Y.-B. Ou, Q.-Y. Wang, Z. Li, L. Wang, Y. Peng, Y. Liu, C. Chen, L. Yu, G. Liu, X. Dong, J. Zhang, C. Chen, Z. Xu, X. Chen, X. Ma, Q. Xue, and X.J. Zhou, *arXiv*:1207.6823.

39. T. Takasaki, T. Ekino, A. Sugimoto, K. Shohara, S. Yamanaka, and A.M. Gabovich, *Euro. Phys. J. B* **73**, 471 (2010).

40. T. Ekino, T. Doukan, and H. Fujii, *J. Low Temp. Phys.* **105**, 563 (1996).

41. T. Ekino, A.M. Gabovich, Mai Suan Li, M. Pękała, H. Szymczak, and A.I. Voitenko, *J. Phys. Condens. Matter* **23**, 385701 (2011).

42. R. Yoshida, T. Wakita, H. Okazaki, Y. Mizuguchi, S. Tsuda, Y. Takano, H. Takeya, K. Hirata, T. Muro, M. Okawa, K. Ishizaka, S. Shin, H. Harima, M. Hirai, Y. Muraoka, and T. Yokota, *J. Phys. Soc. Jpn.* **78**, 034708 (2009).

43. K. Nakayama, T. Sato, P. Richard, T. Kawahara, Y. Sekiba, T. Qian, G.F. Chen, J.L. Luo, N.L. Wang, H. Ding, and T. Takahashi, *Phys. Rev. Lett.* **105**, 197001 (2010).

44. A.M. Gabovich and A.I. Voitenko, *Phys. Rev. B* **56**, 7785 (1997).

45. G. Gruner, *Density Wave in Solids,* Addison-Wesley, Reading, Massachusetts (1994).

46. A.M. Gabovich, A.I. Voitenko, and M. Ausloos, *Phys. Rep.* **367**, 583 (2002).

47. A.M. Gabovich and A.I. Voitenko, *Phys. Rev. B* **75**, 064516 (2007).

48. T.M. McQueen, Q. Huang, V. Ksenofontov, C. Felser, Q. Xu, H. Zandbergen, Y.S. Hor, J. Allred, A.J. Williams, D. Qu, J. Checkelsky, N.P. Ong, and R.J. Cava, *Phys. Rev. B* **79**, 014522 (2009).

49. R. Ukita, A. Sugimoto, and T. Ekino, *Physica C* **471**, 622 (2011).

50. A. Subedi, L. Zhang, D.J. Singh, and M.H. Du, *Phys. Rev. B* **78**, 134514 (2008).